Biophysical Journal, Volume *113*

Supplemental Information

Nanoscale Membrane Budding Induced by CTxB and Detected via Polarized Localization Microscopy

Abir M. Kabbani and Christopher V. Kelly

SUPPLEMENTAL INFORMATION for

Nanoscale membrane budding induced by CTxB on quasi-one component lipid bilayers detected by polarized localization microscopy

A. M. Kabbani and C. V. Kelly

SUPPLEMENTAL MATERIALS AND METHODS

GUV preparation

99.4% POPC, 0.3% GM1, and 0.3% DiI lipids were mixed in chloroform before drying. This composition yielded 110 nm^2 of bilayer per DiI or GM1 molecule. The mixed lipids were then spread uniformly via spin coating on a conducting indium tin oxide (ITO)-coated slide (Sigma-Aldrich). The resulting lipid films were dried under vacuum for one hour. A second ITO-coated slide and silicon spacer enclosed the dried lipids into an incubation chamber. A hydration solution of 200 mM sucrose was added to the dried lipid films and the ITO slides were connected to either side of a sine wave function generator. The growth of the GUVs occurred over 3 hours at 55 °C with an alternating field at 10 Hz and 2 V_{rms}. GUVs were stored at 55°C until use or discarded after 2 days. The interaction between the GUVs and plasma cleaned glass coverslips resulted in bursting of the GUVs and the formation of a continuous SLB over the glass.

Engineered membrane curvature

70 nm radius polystyrene nanoparticles (r_{NP}) of λ_{ex} =488 nm (Fluoro-Max, Fisher Scientific) were exposed to a plasma cleaned coverslip of a glass bottom dish for 10 min to achieve a density of 0.02 NPs/μm^2. Glass bottom dishes were placed on a 55 °C hot plate for 5 min to ensure their stability on the coverslips. The index of refraction of polystyrene is 1.59 and may have resulted in a nanoscale shifting of the localization of single fluorophores, as discussed in the manuscript.

Imaging optics

PLM was performed on an inverted IX83 microscope with Zero-Drift Correction and a 100x, 1.49NA objective (Olympus Corp.) on a vibration-isolated optical table. The high-NA objective permitted through-objective TIRFM. We have incorporated four continuous wave diode lasers at wavelengths 405, 488, 561, and 647 nm with at least 120 mW max power each for fluorescence excitation. The excitation polarization was rotated with a computer-controlled liquid crystal waveplate (Thorlabs Inc, LCC1111-A). Image acquisition was performed with an iXon-897 Ultra EMCCD camera (Andor Technology) proceeded by an OptoSplit IILS (Cairn Research) with emission filters (BrightLine, Semrock, Inc.), a 4-band notch filter (ZET405/488/561/640m, Chroma Corp.), and a 2x magnification lens. This setup provided high power (>80 mW) of linearly polarized fluorescence excitation and integrated computer control of all equipment via custom LabVIEW routines (National Instruments Corp.).

Imaging procedure

For super resolution two-color imaging, samples were exposed to high laser power > 80 mW for excitation wavelengths of λ_{ex} = 561 (DiI) and λ_{ex} = 647 nm (CTxB-AF647) simultaneously. Exposing the sample to high lasers powers for 3 s resulted in converting most of the fluorophores from their fluorescent state '*on*' to the transient non-fluorescent, dark state '*off*' to provide a steady state of well-separated fluorophore blinking. The '*on*' fluorophores were imaged at a density of less than one '*on*' fluorophore/μm^2/frame. Data was acquired simultaneously for p-polarized total internal reflection (TIR) excitation at λ_{ex} = 561 nm for pPLM, and epifluorescence excitation at λ_{ex} = 647 nm for dSTORM. Between 10,000 and 30,000 frames were acquired for each time point at a frame rate of 50 Hz on a region of interest with 18 ms acquisition per frame (t_{exp}).

Single-particle tracking

The sequential fluorophore localizations were linked as a trajectory if they were in sequential frames, within a separation distance of 500 nm, and there was no alternative localization for linking within 2 μm. The single-molecule step lengths (v) were grouped based on their distance from the bud center, and their normalized distribution was fit via non-linear least squares method to a 2D Maxwell-Boltzmann distribution (Eq. S1) as would be expected for 2D Brownian diffusion.

$$P(v) = \frac{v}{2D_{fit}\Delta t} e^{\frac{-v^2}{4D_{fit}\Delta t}}. \quad \text{(Eq. S1)}$$

The localization imprecision increased the apparent step lengths. A camera blur was caused by the single-frame exposure time (t_{exp}) being comparable the time between frames (Δt) (1, 2). The diffusion coefficient (D) was calculated from the D_{fit} of Eq. 2 according to

$$D = (D_{fit} - \frac{\sigma_r^2}{2\Delta t})/(1 - \frac{t_{exp}}{3\Delta t}) \quad \text{(Eq. S2)}$$

with σ_r = 15 nm, Δt = 20 ms, and t_{exp} = 18 ms, if D_{fit} = 0.5 μm^2/s then D = 0.7 μm^2/s or if D_{fit} = 0.1 μm^2/s then D = 0.13 μm^2/s. Since the microscopy methods used here reveal only the *z*-projection of the diffusion, D calculated from Eq. 3 is reported as D_{xy} to emphasize that only the diffusion through the *xy*-plane has been measured. Diffusion coefficients from SPT are typically extracted by fitting the mean squared displacement versus Δt. However, fitting a whole trajectory to a single diffusion coefficient blurs the effects of nanoscale curvature with the lipid trajectory sampling both curved and flat membranes (2). Even with single-step analysis, a single step over 20 ms with a D = 0.55 μm^2/s, as is expected for DiI, would result in the averaging of the membrane environment over the expected 210 nm step length. With greater experimental sampling densities and rates more sophisticated analysis routine would be warranted (2).

PLM detects membrane bending events before epifluorescence and polarized TIRF microscopy

PLM allowed earlier visualization of membrane bending initiated by CTxB than was detectable by epifluorescence and polarized TIRF microscopy. Epifluorescence microscopy revealed a laterally uniform brightness of the DiI and CTxB on the SLB for the first 20 min of CTxB incubation. The formation of CTxB accumulations and lateral DiI variations became evident with epifluorescence microscopy after 20 min in some regions of the sample. Our interpretation of the lateral variations across SLBs and variations between SLBs created by differing methods is discussed in the manuscript. Polarized TIRF microscopy detected regions of membrane bending after ~ 10 minutes of CTxB incubation with the bilayer.

PLM distinguishes between membrane buds and tubules

A membrane that is tilted 0° or 90° relative to the coverslip results in no anisotropic emission effects of the DiI, i.e. no contribution to a systematic shift of the localizations of DiI.

These are the dominant membrane orientations for a membrane tubule topology. Accordingly, the pPLM images of membrane tubules displayed a clear ring-like distribution (Fig. 4). Similarly, the expected localizations of CTxB bound to the outer leaflet of a tubule should exhibit no detected localizations in the center of the tubule since CTxB cannot penetrate the membrane. Scarce localizations in the center of the tubule were presumably due to the undulating motion of the tubule, which resulted in the *z*-projection of DiI molecules within it, yielding localizations across the *xy*-plane (Fig. S3). Further, the probability of exciting a fluorophore with TIR illumination decreases exponentially with distance from the coverslip, which enhances the ring-like structure of acquired localizations. Brief calculations were performed to demonstrate when a ring-like structure would be observed due to the effects of an increase in membrane area and TIR illumination. The simulation incorporated these effects for both cases of membrane buds and membrane tubules of varying heights (Fig. S4). However, the dominant component in DiI localization densities is the coupling between the orientation of the fluorophore, and the polarization of the electric field, as demonstrated previously (3).

Membrane tension affects bud formation

At the location of GUV fusion to the coverslip, and near the center of the SLB patch, there was initially a high concentration of excess membrane from a portion of the GUV or nested GUVs that did not fully fuse to the glass coverslip. These unfused vesicles were removed with vigorous washing to yield an apparently uniform SLB. Membrane buds were most likely to form in the center of the SLB patch, close where the unfused vesicles were, rather than close to the edge of the SLB and the exposed glass coverslip (Fig. S5).

Accordingly, the center of each SLB patch would have a lower membrane tension and encourage bud and tubule formation, as compared to the perimeter of the patch, consistent with our observations.

The rate of GUV bursting was controlled by the duration of plasma cleaning the glass and the presence of a membrane cushion. In the absence of membrane cushion, and under long exposures of plasma cleaning (>2 min), the membrane-substrate adhesion was too strong for the creation of a continuous SLB patch. In this scenario, the GUVs rupture was too vigorous. Diffraction-limited holes in the SLB were observed, and a slower fluorescence recovery times

were measured via fluorescence recovery after photobleaching (FRAP). In these cases, when the membrane-substrate adhesion was too strong, no curvature induction by CTxB was observed.

Bud formation is energetically feasible

The total energetic cost of bending the membrane (E_{Bend}) was estimated via Helfrich energy model (4) for at 50 nm top radius of curvature hemispherical bud with a 20 nm radius of curvature collar smoothly connecting the bud to the surrounding planar SLB (Fig. 1B), such that

$$E_{Bend} = \int (\kappa(H - H_0)^2 + \bar{\kappa}K)dA \, . \qquad \text{(Eq. S3)}$$

This incorporates the membrane bending rigidity (κ), membrane Gaussian curvature modulus ($\bar{\kappa}$), the mean local membrane curvature (H), the local Gaussian curvature (K), the intrinsic membrane curvature ($H_0 \approx 0$), and the area of the bud (A). The bending rigidity of a POPC membrane in TRIS buffer at T = 22°C is $\kappa = (12.9 \pm 0.4) \times 10^{-20}$ J $\approx \bar{\kappa}$ (5, 6). The energy required to bend the membrane into the presumed configuration was calculated analytically $E_{Bend} = (5 \pm 1) \times 10^{-18}$ J.

The adhesion energy of the bilayer to the glass substrate is given by $w = 10^{-8}$ J/m^2 (7). A bottom radius of 67 nm yields 1.4×10^4 nm^2 of the SLB to be separated from the substrate, the energy cost of lifting the membrane off the substrate ($E_{Adhesion}$) equals $(1.4 \pm 1) \times 10^{-22}$ J, which happens to be smaller than $k_BT = 4 \times 10^{-21}$ J.

The intrinsic free energy released per CTxB binding to the GM1 in the SLB is equal to -67 ± 2 kJ/mol (8). The area of the CTxB pentamer is equal to 106 nm^2 and there would be space for 120 CTxB to bind to just the neck region of this membrane bud (9, 10). Accordingly, the energy change upon CTxB accumulating around the neck of this nanoscale bud (E_{Bind}) is $(-1.3 \pm 0.5) \times 10^{-17}$ J.

SUPPLEMENTAL FIGURES

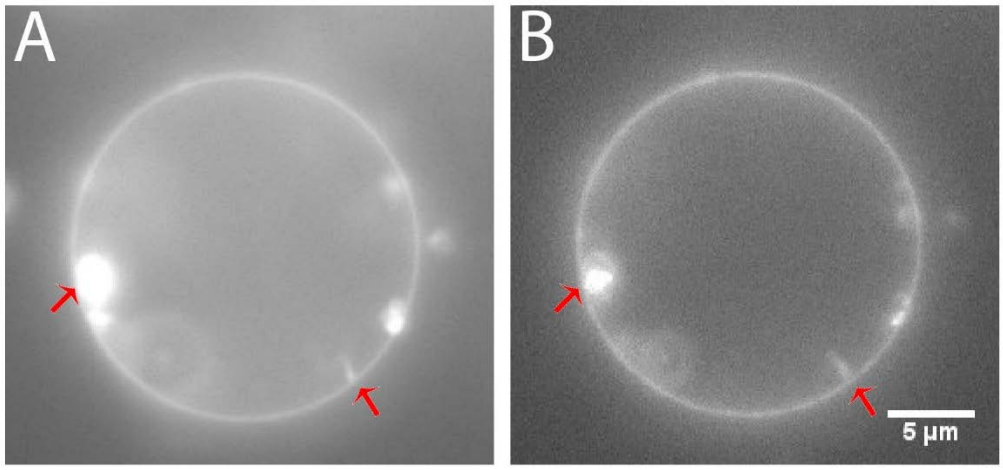

FIGURE S1 CTxB induces vesiculation and inward tubulation in free floating unsupported systems. (A) Giant unilamellar vesicle of 99.6% POPC,0.3% GM1, and 0.3% DiI imaged with λ_{ex} = 561 nm. (B) CTxB channel imaged with λ_{ex} = 647 nm. Red arrows indicate regions of induced curvature and inward invaginations by CTxB.

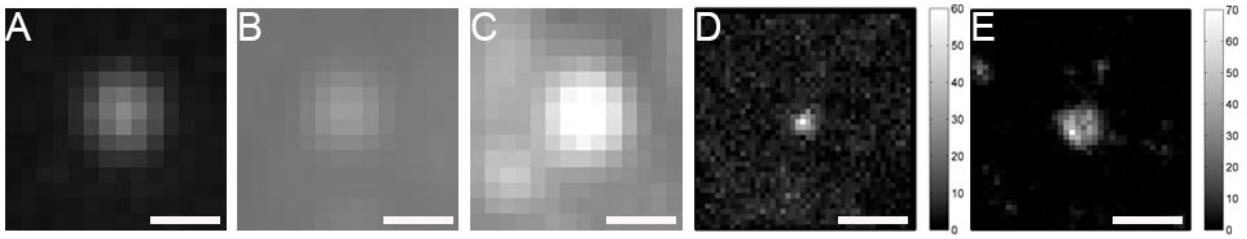

FIGURE S2 CTxB preferentially partitions at negative curvature located at the membrane collar over a 70 nm nanoparticle in radius. Diffraction-limited images of the (A) 70 nm radius nanoparticle imaged with λ_{ex} = 488 nm, (B) pTIRF microscopy image of the membrane, the increase in brightness indicates the presence of curved membrane, and (C) CTxB-AF647 imaged with λ_{ex} = 647 nm showing an increase in brightness at the curved membrane location. (D) 2D histogram plot of localizations from pPLM present increased density of localizations at membrane curvature. (E) 2D histogram plot of localizations obtained from dSTORM results for CTxB demonstrate a clustered localizations around the neck of the curved membrane with a ring-like structure. Scale bars represent (A-C) 0.5 μm and (D,E) 250 nm.

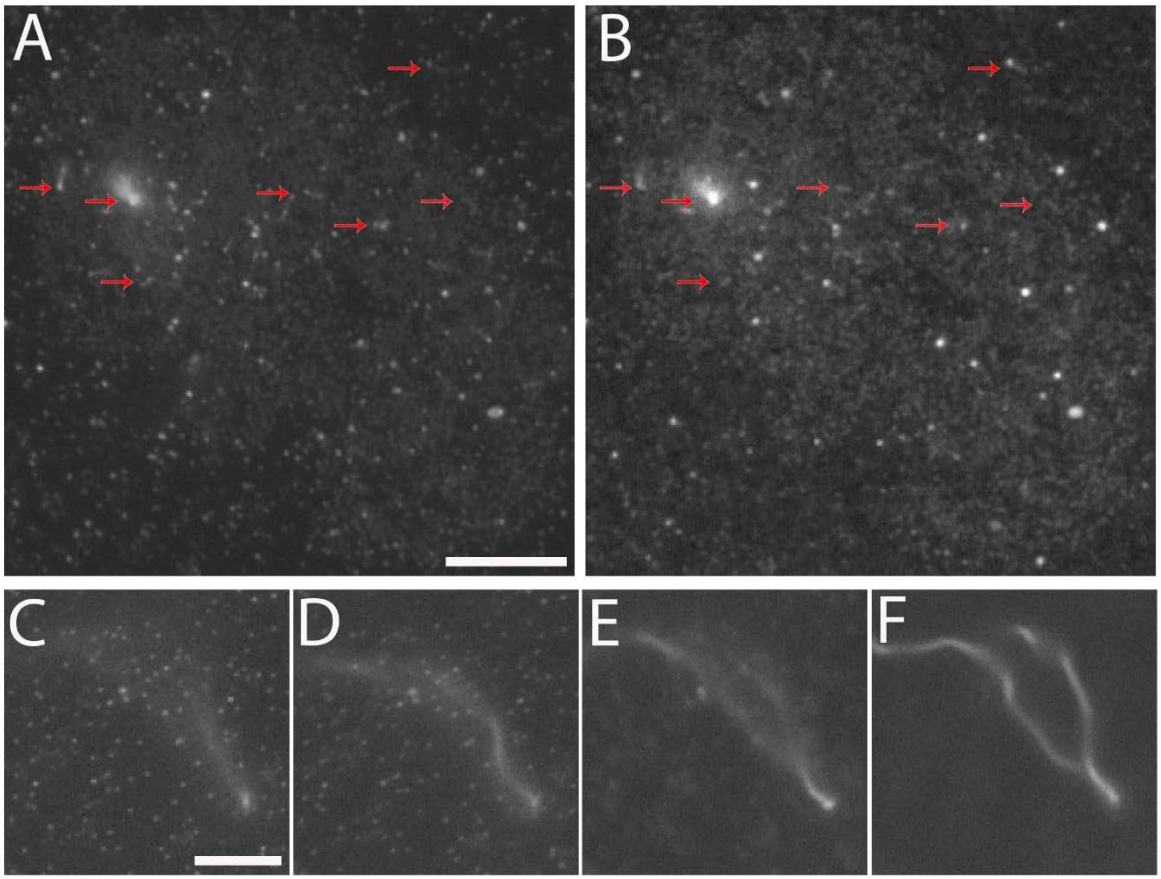

FIGURE S3 CTxB induces budding and tubulation on supported lipid bilayers (POPC/GM1/DiI). (A) Bilayer imaged with epifluorescence after 24 hours of incubation with CTxB. Small membrane buds indicated by regions of spots of increased brightness and long tubules indicated by red arrows appear in the membrane and (B) the CTxB channel. Some tubules extend in length to micron size as observed in (C-F). (C-F) Z-stack image of the membrane tubule protruding from the flat supported bilayer at z = 0, 0.2, 1, and 2 µm, respectively. Scale bars represent 5µm.

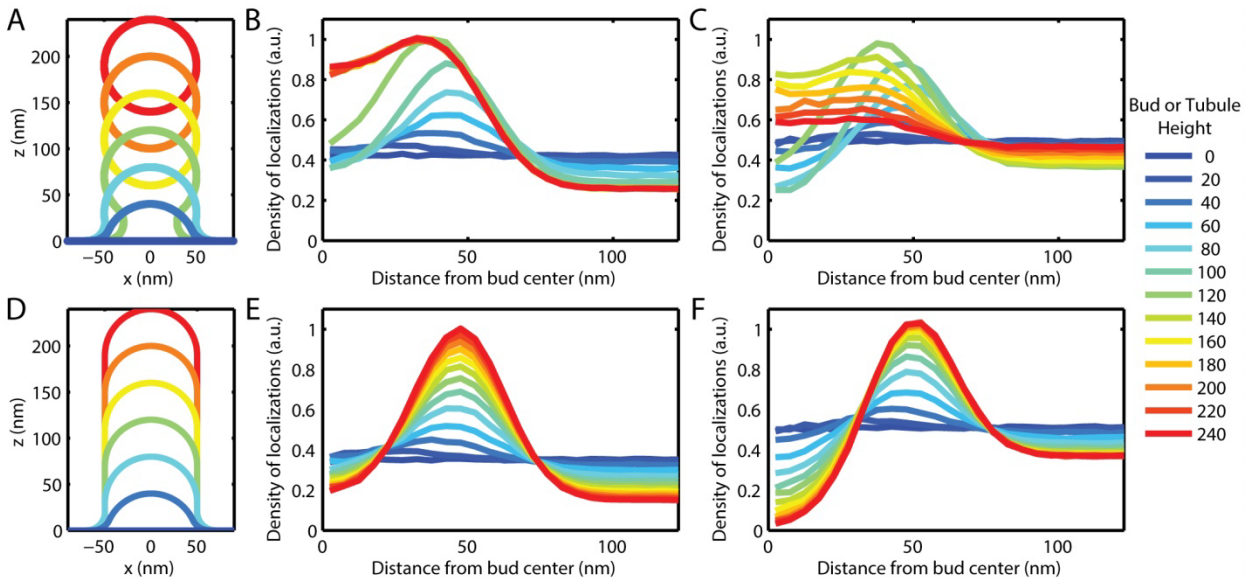

FIGURE S4 The simulated normalized density of localizations versus distance from bud center for (A-C) vesiculation or (D-F) tubulation with varying heights given a bud or tubule diameter of 50 nm. Here, a uniform density of polarization-insensitive membrane-bound probes was simulated across the membrane (*i.e.*, CTxB). The radial densities of localizations with (B, E) epifluorescence illumination or (C, F) TIRF illumination show the illumination conditions and bud height at which the ring-like structure would be observed. (C, F) The observation probability included a characteristic exponential decay length of 124 nm in TIRF illumination which increased the probability of observing a ring in the resulting reconstructed images. A ring-like density of localizations would be observed for vesiculation only when fission is near. A tubule structure would provide a ring-like structure when the bud top is >60 nm above the coverslip. Note, this simulation includes localization uncertainty (σ = 15 nm), but does not incorporate anisotropic emission, as would be the case for polarization-sensitive fluorophores (*i.e.*, DiI).

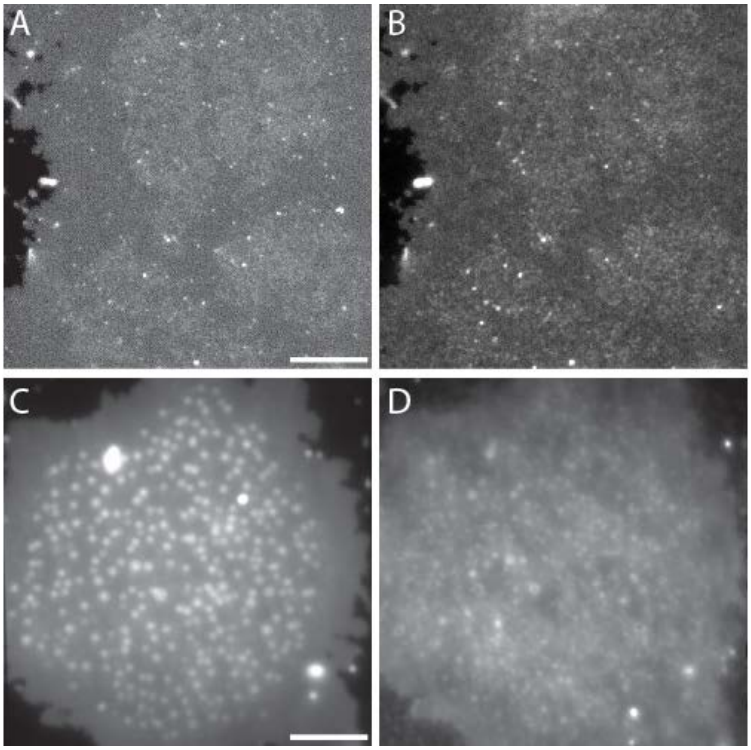

FIGURE S5 Diffraction-limited images of the membrane and bound CTxB. (A, C) a POPC/GM1/DiI membrane with nanoscale membrane budding sites imaged in epifluorescence and p-polarized TIRF, respectively. The buds are detected as a variation of brightnesses across the bilayer, however more prominent in p-polarized TIRF. (B, D) CTxB-AF647 imaged in epifluorescence for the membranes shown in (A) and (C), respectively. Scale bars represent 5 μm.

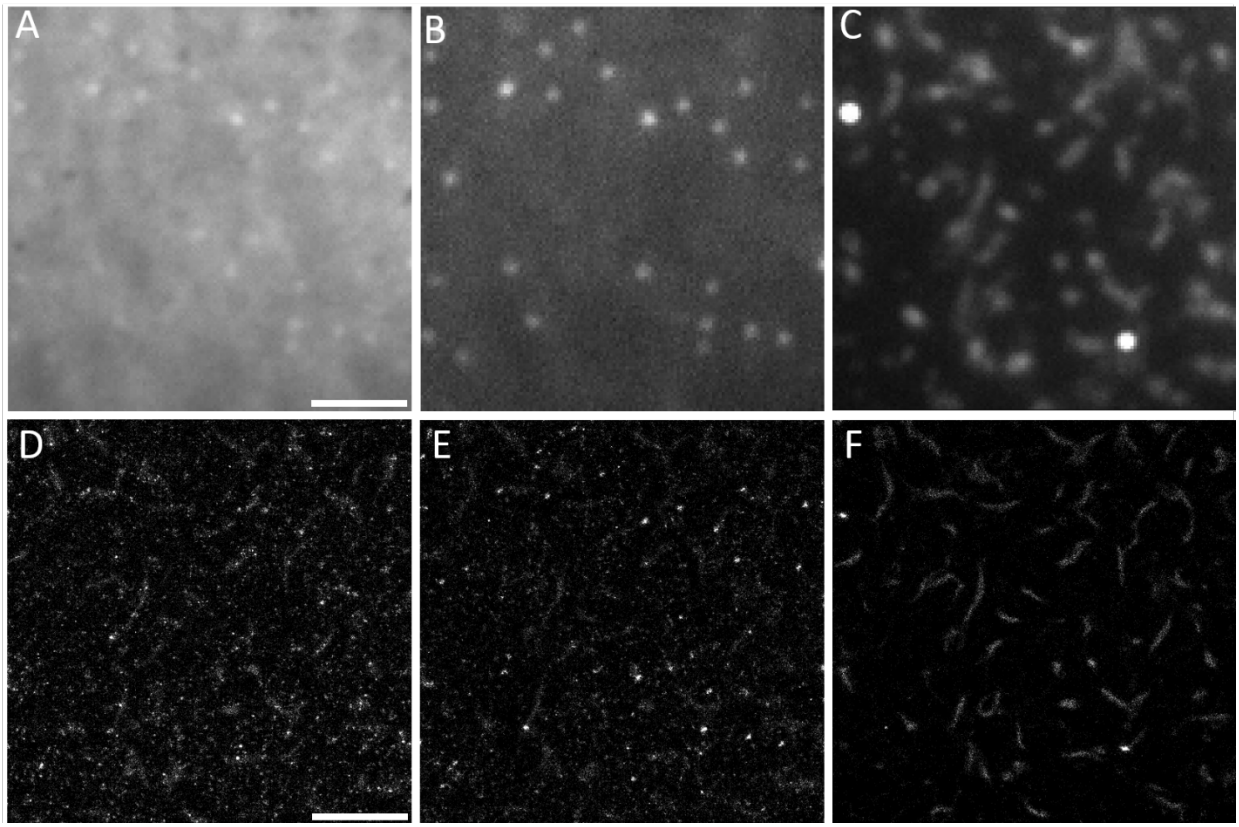

FIGURE S6 CTxB induced membrane ridges and preferentially partitioned at these nanoscale membrane structures. (A-C) Diffraction-limited images of the membrane in sTIRFM, pTIRFM, and the bound CTxB in CTxB channel, respectively. (D, E) Super-resolution reconstructed images plotted as 2D histograms of localizations of the membrane obtained in sPLM, and pPLM, respectively. (F) dSTORM reconstructed image of CTxB-AF647 shows high localization density of CTxB at the induced membrane ridge. The nanoscale size of such membrane structures prohibited their observations in diffracted limited imaging; however, clearly detected in super resolution. Further, CTxB preferentially partitioned to one dimension negative curvature regions observed in these ridges and on wavy glass substrates (11). Only ~4% of 48 samples exhibited nanoscale ridges-induced by CTxB in addition to nanoscale membrane budding. Scale bars in (A-C), and (D-E) represent 4 and 2 μm, respectively.

References:

1. Lagerholm, B.C., D.M. Andrade, M.P. Clausen, and C. Eggeling. 2017. Convergence of lateral dynamic measurements in the plasma membrane of live cells from single particle tracking and STED-FCS. J. Phys. Appl. Phys. 50: 063001.

2. Kabbani, A.M., X. Woodward, and C.V. Kelly. 2017. Resolving the effects of nanoscale membrane curvature on lipid mobility. https://arXiv.org/abs/1706.00087. .

3. Kabbani, A.M., and C.V. Kelly. 2017. The Detection of Nanoscale Membrane Bending with Polarized Localization Microscopy. https://arxiv.org/abs/1703.01498. Biophys J Manuscript Number: 2017BIOPHYSJ307664.

4. Helfrich, W. 1973. Elastic properties of lipid bilayers: theory and possible experiments. Z. Naturforschung Teil C Biochem. Biophys. Biol. Virol. 28: 693–703.

5. Dimova, R. 2014. Recent developments in the field of bending rigidity measurements on membranes. Adv. Colloid Interface Sci. 208: 225–234.

6. Siegel, D.P., and M.M. Kozlov. 2004. The Gaussian Curvature Elastic Modulus of N-Monomethylated Dioleoylphosphatidylethanolamine: Relevance to Membrane Fusion and Lipid Phase Behavior. Biophys. J. 87: 366–374.

7. Tachev, K.D., J.K. Angarska, K.D. Danov, and P.A. Kralchevsky. 2000. Erythrocyte attachment to substrates: determination of membrane tension and adhesion energy. Colloids Surf. B Biointerfaces. 19: 61–80.

8. Turnbull, W.B., B.L. Precious, and S.W. Homans. 2004. Dissecting the cholera toxin-ganglioside GM1 interaction by isothermal titration calorimetry. J. Am. Chem. Soc. 126: 1047–1054.

9. Ewers, H., W. Römer, A.E. Smith, K. Bacia, S. Dmitrieff, W. Chai, R. Mancini, J. Kartenbeck, V. Chambon, L. Berland, A. Oppenheim, G. Schwarzmann, T. Feizi, P. Schwille, P. Sens, A. Helenius, and L. Johannes. 2010. GM1 structure determines SV40-induced membrane invagination and infection. Nat. Cell Biol. 12: 11–18.

10. Pezeshkian, W., A.G. Hansen, L. Johannes, H. Khandelia, J.C. Shillcock, P.B.S. Kumar, and J.H. Ipsen. 2016. Membrane invagination induced by Shiga toxin B-subunit: from molecular structure to tube formation. Soft Matter. 12: 5164–5171.

11. Hsieh, W.-T., C.-J. Hsu, B.R. Capraro, T. Wu, C.-M. Chen, S. Yang, and T. Baumgart. 2012. Curvature Sorting of Peripheral Proteins on Solid-Supported Wavy Membranes. Langmuir. 28: 12838–12843.